JCI insight

# Loss of *ZNF148* enhances insulin secretion in human pancreatic β cells

Eleonora de Klerk, … , Alan D. Attie, Matthias Hebrok

*JCI Insight.* 2023;8(11):e157572. https://doi.org/10.1172/jci.insight.157572.

Research Article | Metabolism | Stem cells

## Graphical abstract

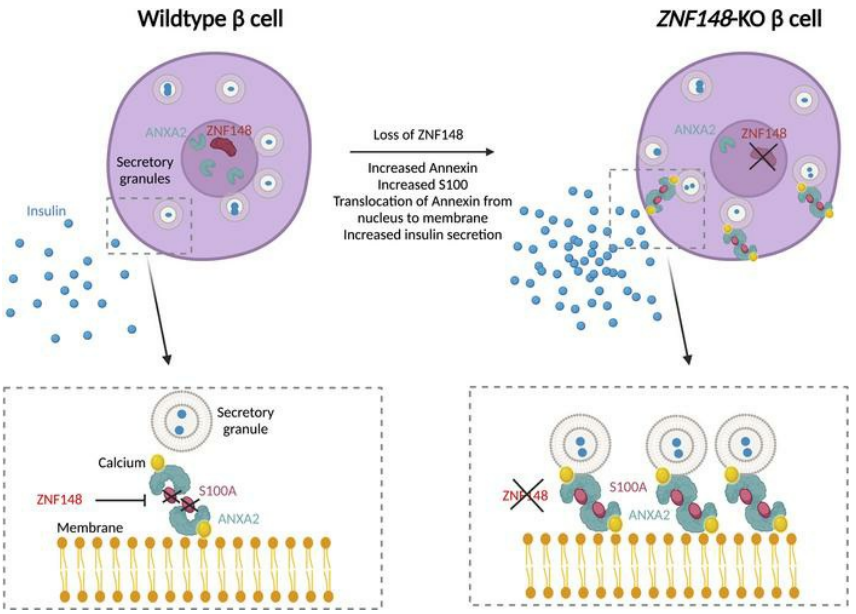


## Find the latest version:

https://jci.me/157572/pdf

JCI insight

RESEARCH ARTICLE

# Loss of *ZNF148* enhances insulin secretion in human pancreatic β cells

**Eleonora de Klerk,[1] Yini Xiao,[1] Christopher H. Emfinger,[2] Mark P. Keller,[2] David I. Berrios,[1] Valentina Loconte,[3,4,5] Axel A. Ekman,[5] Kate L. White,[4,6] Rebecca L. Cardone,[7] Richard G. Kibbey,[7] Alan D. Attie,[8] and Matthias Hebrok[1]**

[1]UCSF Diabetes Center, UCSF, San Francisco, California, USA. [2]Department of Biochemistry, University of Wisconsin-Madison, DeLuca Biochemistry Laboratories, Madison, Wisconsin, USA. [3]Department of Anatomy, School of Medicine, UCSF, San Francisco, California, USA. [4]Molecular Biophysics and Integrated Bioimaging Division, Lawrence Berkeley National Laboratory, Berkeley, California, USA. [5]National Center for X-ray Tomography, Advanced Light Source, Berkeley, California, USA. [6]Department of Chemistry, Bridge Institute, Michelson Center for Convergent Bioscience, University of Southern California, Los Angeles, California, USA. [7]Department of Internal Medicine (Endocrinology), Yale University, New Haven, Connecticut, USA.[8]Departments of Biochemistry, Chemistry, and Medicine, University of Wisconsin-Madison, DeLuca Biochemistry Laboratories, Madison, Wisconsin, USA.

**Insulin secretion from pancreatic β cells is essential to the maintenance of glucose homeostasis. Defects in this process result in diabetes. Identifying genetic regulators that impair insulin secretion is crucial for the identification of novel therapeutic targets. Here, we show that reduction of *ZNF148* in human islets, and its deletion in stem cell–derived β cells (SC-β cells), enhances insulin secretion. Transcriptomics of *ZNF148*-deficient SC-β cells identifies increased expression of annexin and S100 genes whose proteins form tetrameric complexes involved in regulation of insulin vesicle trafficking and exocytosis. ZNF148 in SC-β cells prevents translocation of annexin A2 from the nucleus to its functional place at the cell membrane via direct repression of *S100A16* expression. These findings point to *ZNF148* as a regulator of annexin-S100 complexes in human β cells and suggest that suppression of *ZNF148* may provide a novel therapeutic strategy to enhance insulin secretion.**

## Introduction

Insulin secretion from pancreatic β cells maintains blood glucose levels within a narrow physiological range. Loss of β cell number and/or function results in type 1 and type 2 diabetes mellitus (T1D, T2D). Stem cell–based replacement therapy is emerging as an alternative to cadaveric islet or whole pancreas organ transplantation (1). Replicating the precise regulation of insulin secretion of endogenous β cells is essential in ensuring safety and functionality of stem cell–derived β cells (SC-β cells). Many of the current SC-β cells (2–11) lack the ability to fully recapitulate the magnitude and biphasic pattern of secretion (12), consisting of a transient acute release (first phase) followed by a sustained secondary release (second phase). This biphasic nature is derived, in part, from distinct intracellular localization of insulin granules whose movement is coupled to reorganization of the cytoskeleton.

Annexins are membrane-binding proteins involved in trafficking events, including formation of linkages between membranes and cytoskeleton, movement of intracellular vesicles, and $Ca^{2+}$-regulated exocytosis (13–16). In particular, annexin 1 (ANXA1) is known to regulate second-phase insulin secretion (17), and ANXA2 is involved in actin-dependent vesicle transport (18–21). Annexins respond to increased $[Ca^{2+}]_i$ by shuttling between the nucleus and the plasma membrane (22). Cellular localization of annexins is mediated via formation of heterotetrameric complexes through binding to the S100 protein family (15, 23). S100-ANXA complexes have been implicated in the fusion of intracellular vesicles to membranes, and organization of membrane-cytoskeleton contacts (24, 25).

Determining genetic regulators that control the amplitude and the biphasic nature of insulin secretion is crucial for the generation of SC-β cells that closely resemble primary β cells and for the development of therapies that aim at improving endogenous islet function.

*ZNF148* is a Krüpple-like zinc finger transcription factor recently identified by us as a negative regulator of insulin secretion in rodents (26). Known to both enhance and repress gene expression (27–29),

**Conflict of interest:** MH holds stocks in Encellin Inc. and Thymmune Therapeutics Inc. and has received research support from Eli Lilly. He is the cofounder and SAB member of Minutia Inc. and holds stocks and options in the company.



**Submitted:** December 14, 2021
**Accepted:** April 5, 2023
**Published:** May 22, 2023

**Reference information:** *JCI Insight*. 2023;8(10):e157572. https://doi.org/10.1172/jci.insight.157572.

*ZNF148* was initially identified for its roles in T cell receptor modulation (30), gastrin expression (28), cancer (31), and skeletal muscle differentiation (32). Single-nucleotide polymorphisms (SNPs) harboring *ZNF148*, including several 3′-UTR variants associated with T2D with an allele frequency of 0.36, have been identified (https://t2d.hugeamp.org). Of note, several variants within the *ZNF148* gene are associated with fasting insulin, glucose, and HOMA-IR (26).

Here, we report that reduction of *ZNF148* in primary human islets enhances insulin secretion. Similarly, loss of *ZNF148* in human SC–β cells enhances insulin secretion and impacts distribution of insulin granules. Transcriptomic analysis in SC–β cells depleted of *ZNF148* reveals an increased expression of genes coding for proteins localized in secretory granules and an enrichment of calcium binding proteins, including members of the annexin and the S100 families. ZNF148 directly binds to the promoter region of *S100A16* in human islets, and deletion of the transcription factor in SC–β cells results in upregulation of S100A16 and translocation of ANXA2 to the cell membrane, thus restoring membrane dynamics to be similar to those observed in endogenous human islets. Overall, our data indicate that reduction of ZNF148 improves insulin secretion properties of both SC–β cells and endogenous islet β cells, suggesting a role for *ZNF148* as a promising therapeutic target.

## Results

*ZNF148 is not required for β cell specification*. *ZNF148* is a ubiquitous transcription factor highly expressed in human and mouse (33) pancreatic β cells. Although several SNPs are associated with T2D (https://t2d.hugeamp.org), its role in human islet function is largely unknown. We (26) recently discovered a link between insulin secretion and a locus that includes the mouse ortholog *Zfp148* in a genetic screen performed on islets isolated from Diversity Outbred mice, an outbred stock that represents as much genetic variation as is present in the human population. The expression of *Zfp148* is negatively correlated with glucose-stimulated insulin secretion (GSIS), and mice with a β cell–specific deletion of *Zfp148* displayed improved glucose tolerance and enhanced insulin secretion.

To characterize the role of *ZNF148* during the specification of human β cells, we employed our stem cell–to–β cell differentiation model system (Figure 1A) (3). We first measured the expression of *INS* during the course of pancreas and endocrine differentiation (Figure 1, B–D). INS gene expression increased sharply after the first 12 days of differentiation when endocrine and β cell progenitors become specified (Figure 1B). In contrast, the expression of *ZNF148* remained stable during β cell specification, as progenitor cells and immature β-like cells expressed similar levels of *ZNF148* (Figure 1C).

Our prior work has shown that isolation of insulin$^+$ cells (INS$^{GFP/w}$; ref. 3) by FACS followed by reaggregation stimulates maturation of β cells and results in enriched β cell clusters (eBC) (Figure 1A). Transcriptomic analysis comparing immature β-like clusters and maturing eBC through bulk RNA-Seq (3) did not reveal major changes in *ZNF148* expression, and *ZNF148* expression in maturing eBC was similar to that in isolated β cells from human islets (3) (Figure 1D). Immunostaining analysis of eBC confirmed nuclear expression of ZNF148 protein in SC–β cells (Figure 1E).

To explore whether expression of *ZNF148* is confined to specific subpopulations, we identified *ZNF148*$^+$ cells by single-cell RNA-Seq in immature β-like clusters and eBC (Figure 1, F and G). Cells within the immature β-like clusters are heterogeneous, containing both nonendocrine and endocrine cells, with 45%–60% of them being positive for C-peptide (C-PEP$^+$). Although enriched for INS/GFP$^+$ cells, eBC also contain subpopulations of bihormonal cells, including C-PEP$^+$/GCG$^+$ and C-PEP$^+$/SST$^+$, which further differentiate into α-like and δ-like cells once transplanted in vivo (3). Single-cell analysis showed that expression of *ZNF148* is not confined to a specific endocrine compartment, neither in immature β cell clusters (Figure 1F) nor in maturing eBC (Figure 1G). These results are comparable with what has been reported for endogenous human islets (34), where expression of *ZNF148* is found in the endocrine subpopulation, as well as what has been reported for acinar cells. Overall, these data demonstrate that the *ZNF148* expression patterns in our SC–β cell model resemble expression in human islets and that expression of *ZNF148* does not correlate with insulin expression during endocrine specification.

To investigate whether loss of ZNF148 alters β cell specification in human SC–β cells, we used CRISPR-Cas9 to generate 2 homozygous KO ZNF148 genes in embryonic stem cell lines (*ZNF148*-KO clone A and B) (Figure 2A and Supplemental Figure 1; supplemental material available online with this article; https://doi.org/10.1172/jci.insight.157572DS1). Bulk RNA-Seq analysis of *ZNF148*-KO eBC showed decreased expression of the edited *ZNF148* (Figure 2B) (most likely due to mRNA instability),

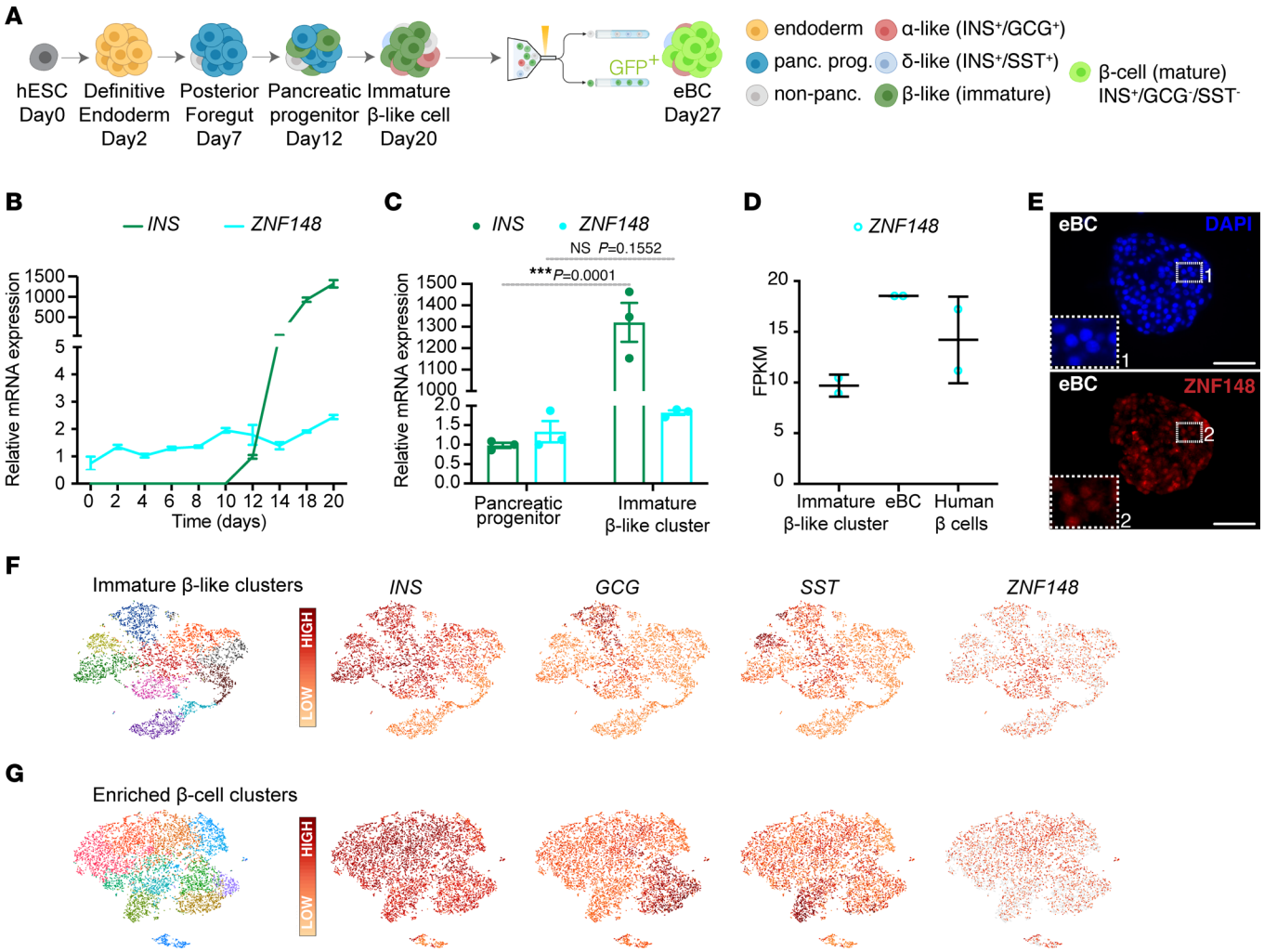


**Figure 1. Characterization of *ZNF148* expression during SC–β cell differentiation.** (**A**) Schematic representation of the differentiation process from hESC (day 0) to eBC (day 27). (**B**) qRT-PCR time course expression analysis of *ZNF148* and *INS* from undifferentiated hESCs (day 0) to immature β-like clusters (day 20). Data for *ZNF148* and *INS* are presented as mean fold change relative to day 0 and to day 12, respectively; $n = 3$ independent and $n = 2$ technical samples. (**C**) qRT-PCR for *ZNF148* and *INS* mRNA in pancreatic progenitors (day 12) and immature β-like clusters (day 20). Data presented as mean fold change relative to day 12; $n = 3$ independent and $n = 2$ technical samples. Data are presented as mean ± SEM. ***$P < 0.001$ determined by 2-tailed Student's $t$ test. (**D**) FPKM values from RNA-Seq data for *ZNF148* mRNA in immature β-like clusters (day 20), eBC (day 27), and endogenous β cells isolated from human islets by fluorescence-activated cell sorting (FACS). Data presented as mean ± SD; $n = 2$ independent samples. (**E**) Immunofluorescent staining of ZNF148 (red) in eBC. DAPI depicts nuclei (blue). Scale bar: 50 μm. (**F** and **G**) t-Distributed stochastic neighbor embedding algorithm (t-SNE) analysis from scRNA-Seq of immature β-like clusters (**F**) and eBC (**G**). Cells expressing *INS*, *GCG*, *SST*, and *ZNF148* are shown in separate plots, with expression levels shown as heatmap of log2 expression. Expression levels in β-like clusters: *INS* log2 expression (min 3.3, max 12.2), *GCG* log2 expression (min 0, max 12.4), *SST* log2 expression (min 1, max 13.6), *ZNF148* log2 expression (min 1, max 3). Expression levels in eBC: *INS* log2 expression (min 5.3, max 12.4), *GCG* log2 expression (min 0, max 12.4), *SST* log2 expression (min 2.3, max 13.3), *ZNF148* log2 expression (min 0, max 2.8). NS, not significant.

and immunostaining analysis confirmed the loss of ZNF148 protein in both clones (Figure 2C). To assess whether *ZNF148* elimination impairs endoderm or pancreatic specification, we conducted flow cytometry and quantitative PCR (qPCR) analysis of immature β-like clusters. Neither differences in the percentage of INS/GFP$^+$ cells (Figure 2D) nor changes in insulin mRNA levels were observed (Figure 2E). Both *ZNF148*-KO clones generated comparable immature β-like clusters (~45 % INS/GFP$^+$ cells) and, thus, were used interchangeably for further analysis. Flow cytometry analysis of β cell markers showed that percentages of C-PEP$^+$, NKX6.1$^+$, PDX1$^+$, and C-PEP$^+$/NKX6.1$^+$ double-positive cells resembled those of control clusters (Figure 2, F and G). Immature *ZNF148*-KO clusters were indistinguishable from immature control clusters also in morphology and size (Figure 2H). Taken together, these data suggest that *ZNF148* is not required for β cell specification.

*Loss of ZNF148 affects the kinetics of insulin secretion in SC–β cells.* To investigate whether loss of *ZNF148* enhances insulin secretion in human SC–β cells similarly to what has been observed in rodents

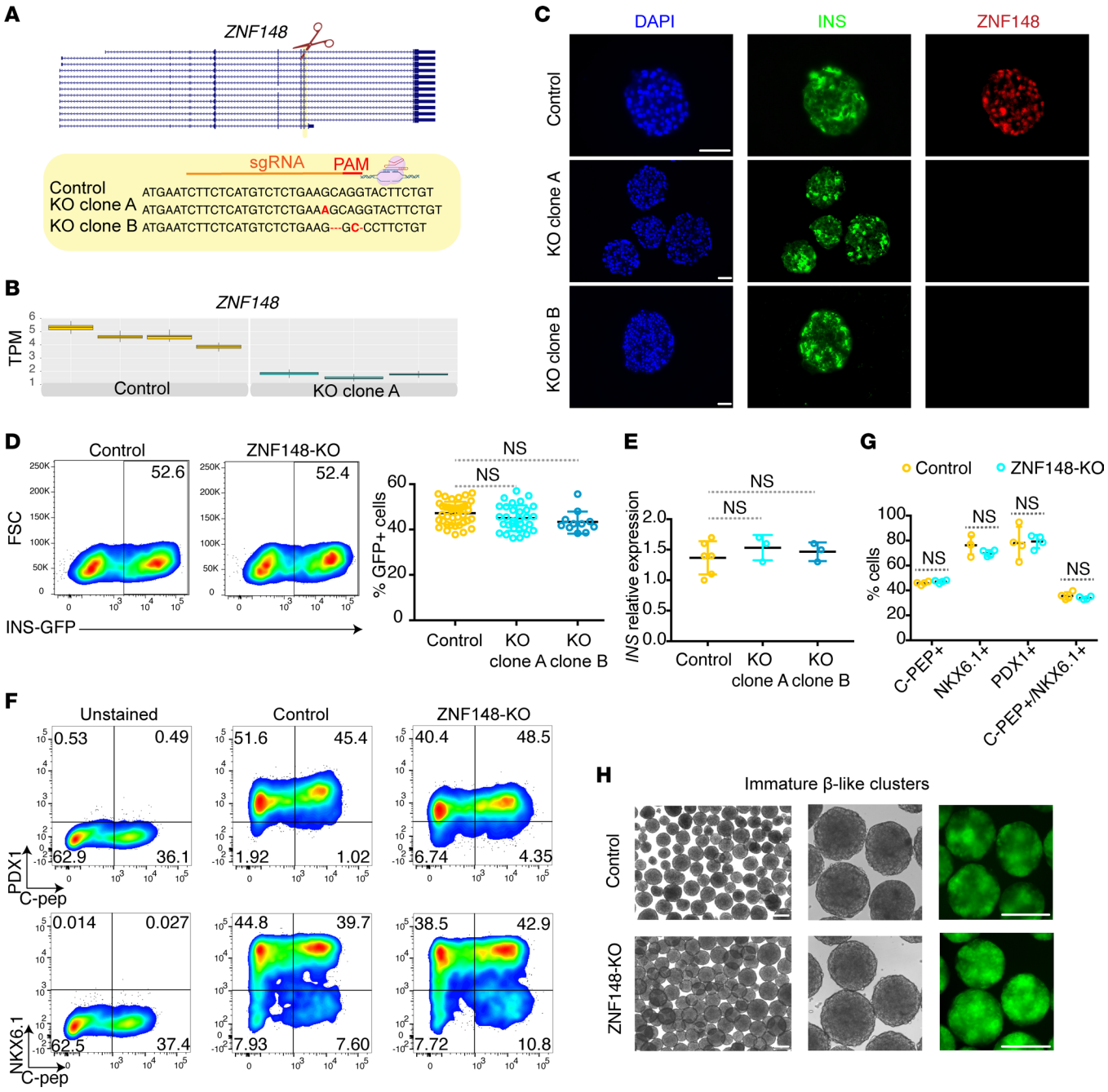


**Figure 2. *ZNF148* is not required for β cells specification.** (**A**) Schematic view of *ZNF148* mRNA variants, and sgRNA sequence targeting exon 7. Edited sequences from *ZNF148*-KO clone A and clone B lines are displayed below, with indels in red. (**B**) RNA-Seq measurement of *ZNF148* (transcripts per million) in unedited (gold) and edited (cyan) eBC (clone A). (**C**) Immunofluorescence staining of ZNF148 (red) and INS (green) in immature β-like clusters (day 20). DAPI staining depicts nuclei (blue). Scale bar: 50 μm. (**D**) Representative image of flow cytometry quantification of GFP$^+$ live cells in control β-like clusters and *ZNF148*-KO clusters (clone A) (left panels), and quantitative analysis indicating percentage of GFP$^+$ cells in control and *ZNF148*-KO β-like clusters (clone A and B) (right panel). $n$ = 11–37. (**E**) *INS* mRNA expression levels in control and *ZNF148*-KO β-like clusters (clone A and B) as measured by qPCR. $n$ = 3–6. (**F**) Representative image of flow cytometry quantification of C-PEP$^+$, NKX6.1$^+$, PDX1$^+$, C-PEP$^+$/NKX6.1$^+$, and C-PEP$^+$/PDX1$^+$ double-positive cells in control and *ZNF148*-KO β-like clusters (clone A). (**G**) Quantitative flow cytometry analysis indicating percentage of C-PEP$^+$, NKX6.1$^+$, PDX1$^+$, and C-PEP$^+$/NKX6.1$^+$ double-positive cells in control and *ZNF148*-KO β-like clusters (clone A). $n$ = 4. (**H**) Bright-field and fluorescence representative images of control and *ZNF148*-KO (clone A) β-like clusters (day 20). Scale bar: 200 μm.

(26), we measured GSIS in *ZNF148*-KO eBC. Maturing *ZNF148*-KO eBC were indistinguishable in morphology and size from control clusters (Figure 3A). Flow cytometry analysis demonstrated that *ZNF148*-KO eBC contained similar percentages of C-PEP$^+$/PDX1$^+$ double-positive cells (>70%) and C-PEP$^+$/NKX6.1$^+$ double-positive cells (>65%) (Figure 3, B and C). Despite these similarities,

*ZNF148*-KO eBC secreted approximately 3 times more C-PEP when challenged with high glucose (Figure 3D) in static conditions. The increase in C-PEP secretion was not observed during the acute first-phase response as measured by dynamic GSIS (Figure 3E) and was independent from the total level of C-PEP (data not shown). Instead, dynamic perifusion revealed an alteration in the kinetics of insulin secretion (Figure 3F; minute 20–50 corresponds to 20 mM high glucose; minute 20–30 corresponds to first phase secretion). Specifically, C-PEP release was sustained after the acute response, and an earlier rise in secretion was observed after membrane depolarization induced by KCl challenge. This phenotype partially recapitulates the observations in β cell–specific *Zfp148*-knockout (*β-Zfp148*$^{KO}$) mice (26), where both first- and second-phase secretion are enhanced.

We next asked whether the absence of enhanced insulin secretion during the acute first phase in *ZNF148*-KO eBC was the result of a metabolic bottleneck previously reported by Davis and colleagues (35). Davis and colleagues showed that GSIS is deficient in SC–β cells maintained in vitro. This deficiency is attributed to a disconnect between early and late stages of glycolysis as well as a reduction of total phosphoenol pyruvate (PEP) derived from oxaloacetate in the mitochondria (Supplemental Figure 2A). To test if our in vitro SC–β cell model shares the impairment in glucose metabolism, we performed mass spectrometry analysis to measure the relative abundance of 3-phosphoglycetate (3PG), PEP, and pyruvate in control eBC incubated in stimulatory glucose (8 mM or 20 mM) and compared the relative abundance to previously published data from endogenous human islets (35). While high glucose elevates the relative abundance of 3PG, PEP, and pyruvate in human islets, no increase was observed in control eBC (Supplemental Figure 2E) or *ZNF148*-KO eBC incubated at stimulatory glucose (20 mM) (Supplemental Figure 2F). To further probe quantitative changes in metabolites, we then performed steady-state stable isotope labeling studies using uniformly labeled $^{13}$C glucose followed by mass isotopomer multiordinate spectral analysis (MIMOSA) as previously described (35, 36). When tracking the atomic percent enrichments (APE) of labeled glucose ($^{13}$C) through glycolysis and tricarboxylic acid cycle (TCA), a significant dilution of label was observed when entering the TCA cycle, both for control and *ZNF148*-KO eBC (Supplemental Figure 2B). We also observed a significant reduction in metabolite tracer accumulation in malate from anaplerotic generation of oxaloacetate (indicated as malate M+3) and $^{13}$C accumulation in PEP derived from oxaloacetate (indicated as PEP M+2) (Supplemental Figure 2, C and D) as previously shown by Davis and colleagues (35). This reduction results in a decrease of PEP derived from mitochondria, an essential metabolite for proper insulin secretion in human islets (37). Overall, we did not note differences in malate M+3 and PEP M+2 concentrations between *ZNF148*-KO eBC and controls (Supplemental Figure 2D). Thus, loss of *ZNF148* does not rescue the inherent deficiency in SC–β cell glucose metabolism in vitro. Although these defects pose a block in first-phase insulin secretion, the positive effects of *ZNF148* loss on insulin secretion in SC–β cells are observed when measuring overall secretion (Figure 3, D and F).

Another critical component of GSIS is robust stimulation of cytosolic calcium flux and coordinated oscillatory [$Ca^{2+}$] responses. Our previous work demonstrate that eBC are capable of increasing calcium influx (3); however, we did not quantify the extent to which individual cells activate a calcium response and whether a coordinated cluster-wide oscillatory pattern is present. Of note, $Ca^{2+}$ dynamics in isolated human islets are different from those observed in isolated rodent islets (38). In rodent islets, coordinated [$Ca^{2+}$] activity occurs over most of the islet area. In contrast, prior work has shown that, in human islets, only a minority (3 of 40 islets) showed oscillations similar to those from rodents, while the majority of the islets displayed coordinated synchronous [$Ca^{2+}$] oscillations in only ~30% of the total islet area (38). The restriction of oscillations to subregions of a given islet is also observed in our stem cell–derived eBCs (Supplemental Figure 3). In addition to measuring the overall increase in calcium influx upon glucose stimulation in *ZNF148*-KO eBC (Supplemental Figure 3A), we specifically analyzed the underlying oscillatory patterns in SC–β cells. The glycolytic bottleneck poses some challenges in the assessment of the oscillatory behaviors. Nevertheless, our data suggest that, while a limited response in just a few β cells was observed in control eBC, a larger percentage of β cells displayed active calcium influx in *ZNF148*-KO eBC (Supplemental Figure 3, D and E). In addition, control eBC mainly displayed unsynchronized oscillations in isolated regions of the clusters (referred to as focal responses) (Supplemental Figure 3, B and C), while *ZNF148*-KO eBC displayed more coordinated oscillations (both with multiple and single pulses; Supplemental Figure 3C, right panel) in a higher fraction of eBC. Taken together, these data suggest that loss of *ZNF148* strengthens coordinated $Ca^{2+}$ dynamics and positively regulates insulin secretion.

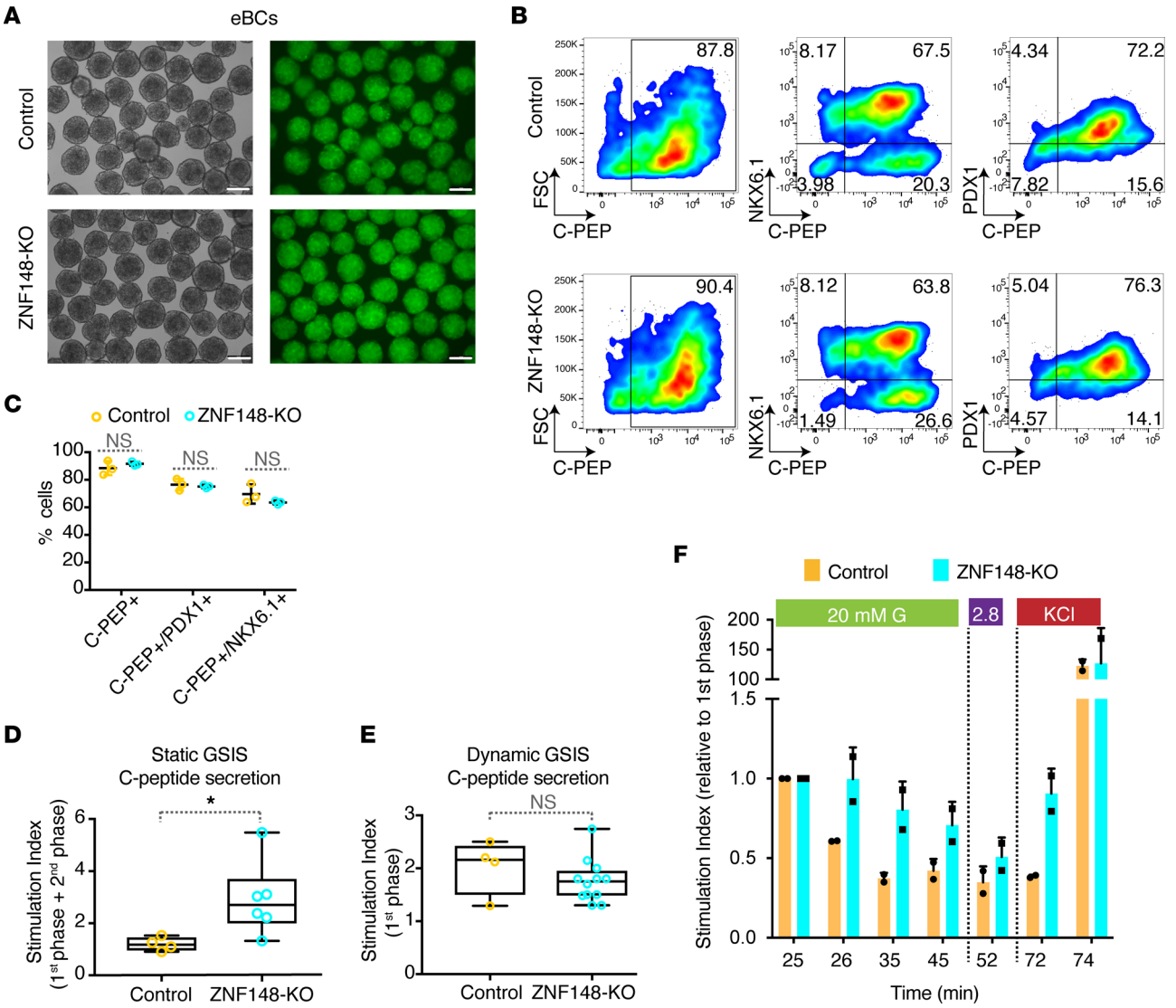


**Figure 3. Loss of *ZNF148* affect kinetics of insulin secretion in SC-β cells.** (**A**) Bright-field and fluorescence representative images of control and *ZNF148*-KO (clone A) eBCs. Scale bar: 200 μm. (**B**) Flow cytometry quantification of C-PEP$^+$, NKX6.1$^+$, PDX1$^+$, C-PEP$^+$/NKX6.1$^+$, and C-PEP$^+$/ PDX1$^+$ double-positive cells in control and *ZNF148*-KO (clone A) eBC. (**C**) Quantitative flow cytometry analysis indicating percentage of C-PEP$^+$, C-PEP$^+$/NKX6.1$^+$, and C-PEP$^+$/ PDX1$^+$ double-positive cells in control and *ZNF148*-KO eBC (clone A). $n = 3$. (**D**) Static GSIS of control and *ZNF148*-KO eBC. Data are presented as stimulation index, corresponding to mean ± SD of fold change (C-peptide secretion at 20 mM glucose over 2.8 mM glucose). $n = 4$–6. $^*P < 0.05$ determined by 2-tailed *t* test. (**E**) Dynamic GSIS of control and *ZNF148*-KO eBC during the first phase secretion (minute 20–25). Data are presented as stimulation index, corresponding to mean ± SD (fold change relative to 2.8 mM glucose). $n = 4$–12. (**F**) Dynamic glucose-stimulated insulin secretion of control and *ZNF148*-KO eBC. Data are presented as stimulation index relative to minute 25, corresponding to the acute phase in insulin release. $n = 4$–6. $^*P < 0.05$ determined by 2-tailed *t* test.

*Loss of ZNF148 increases expression of annexins and S100 genes in SC-β cells.* To further explore the mechanism by which *ZNF148* affects insulin secretion, we profiled gene expression in control and *ZNF148*-KO eBC, identifying ~1,000 differentially expressed genes ($q < 0.05$) (Supplemental Table 1). Cellular component Ontology analysis (Figure 4A and Supplemental Table 2) identified secretory granule lumen (https://www.ebi.ac.uk/QuickGO/term/GO:0034774) and cytoskeleton (https://www.ebi.ac.uk/QuickGO/term/GO:0005856) as the top 2 enriched categories (in terms of subcellular areas) within the differentially regulated genes. Gene enrichment analysis based on KEGG (Figure 4B and Supplemental Table 3) identified proteoglycans (https://www.genome.jp/dbget-bin/www_bget?pathway:hsa05205), axon guidance (https://www.genome.jp/entry/pathway+hsa04360), and gap junctions (https://www.genome.jp/dbget-bin/www_bget?pathway+hsa04540) as the most highly enriched pathways. Gene sets enriched for axon guidance included those associated with the actin cytoskeleton pathway (https://www.genome.jp/entry/hsa04810), while those enriched for gap junctions included genes

linked to calcium signaling (https://www.kegg.jp/entry/hsa04020). Several differentially regulated genes in the *ZNF148*-KO eBC (Figure 4C) have been previously linked to insulin secretion, including *GSN* (39), *TAGLN* (40), and *RHOC* (41) (cytoskeleton remodeling); *AHNAK* (20) and *FKBP1B* (42) (calcium flux); *KCNA3* (43) (membrane polarization); *VAMP8* (44) and *ANXA1* (45) (vesicles exocytosis); *SEC11C* (46) (insulin processing); and *UCN3* (47, 48) (β cell maturation). *SPP1* (49), *CHTS* (50), and *PLCXD3* (51) have also been implicated in insulin secretion, but the exact molecular mechanism has not yet been entirely elucidated.

Calcium binding was the most highly enriched Gene Ontology (GO) molecular function (Figure 4D and Supplemental Table 4) and included members of the annexin family and the S100 families (Supplemental Table 5). Four members of the annexin family (*ANXA1*, *ANXA2*, *ANXA3*, and *ANXA4*) and 5 members of the S100 family (*S100A7*, *S100A9*, *S100A10*, *S100A11*, and *S100A16*) all showed increased expression in the *ZNF148*-KO eBC (Figure 4, C and F). Functional annexin-S100 complexes have been recognized as regulators of calcium flux (Figure 4E), and annexin proteins are known to be involved in trafficking events, including movement of intracellular vesicles and $Ca^{2+}$-regulated exocytosis (13–16).

Annexins are known to be expressed in the endocrine compartment of human islets (34). Comparative RNA-Seq analysis of control eBC and isolated endogenous human β cells revealed differences in the expression levels of several annexin proteins (*ANXA1*, *ANXA2*, and *ANXA4*), with *ANXA2* being the most highly expressed in endogenous human β cells at a level that is ~400-fold higher than that observed in control eBC (Figure 4G). The expression of *ANXA2* differed in our eBC not only in terms of RNA levels but also in terms of cell type specificity. While previously published single-cell data on human islets (34) have shown expression of *ANXA2* in every endocrine subpopulation and in most of the cells included in the β cell cluster (Figure 4H, bottom panel), the expression of *ANXA2* in control eBC was mainly confined to a separate subpopulation (Figure 4H, top panel) characterized by cells expressing lower levels of insulin (Figure 1G). In contrast, expression of both annexin and S100 genes was increased in *ZNF148*-KO eBC (Figure 4, F and I), consistent with a link between ZNF148 and insulin vesicle trafficking and secretion via regulation of the annexin family.

*Loss of ZNF148 restores translocation of annexins to cellular membranes in SC–β cells.* Annexins link $Ca^{2+}$ signaling and membrane functions as they relocate from within nuclei to the nuclear and plasma membrane in response to elevated $[Ca^{2+}]_i$ (15, 22). Cellular translocation requires the formation of heterotetrameric complexes with members of the S100 family; these complexes regulate the organization of membranes and vesicles and have been involved in fusion of vesicles with the plasma membrane (24). Because of the elevated expression of *S100A7*, *S100A9*, *S100A10*, *S100A11*, and *S100A16* in *ZNF148*-KO eBC (Figure 4F), we asked if cellular localization of ANXA2 was altered in *ZNF148*-KO eBC. Immunostaining analysis of ANXA2 revealed predominant expression in the nuclei of control eBC, whereas in *ZNF148*-KO eBC, ANXA2 was localized throughout the cell, with highest levels found at the plasma membrane (Figure 5, A and B). Notably, we observed an even higher abundance of membrane-associated ANXA2 along the periphery of *ZNF148*-KO eBC clusters. Immunostaining was performed on tissue sections of eBC, thus excluding permeation issues as a reason for the staining at the periphery of the clusters. Immunostaining analysis was also performed for *ANXA1* and *ANXA3* (Supplemental Figure 4). *ANXA1* displayed a pattern similar to *ANXA2*, in which *ZNF148*-KO eBC showed *ANXA1* expression mainly at the plasma membranes, and increased expression was also found in some cells located at the periphery of the cluster. In contrast, *ANXA3* was mainly detected in the cytoplasm in both control and *ZNF148*-KO eBC.

Considering that most of the dramatic changes in expression and cellular location were observed for ANXA2, we explored its protein expression pattern in endogenous human islets. Immunostaining of human pancreatic sections from 5 different donors revealed that *ANXA2* is highly expressed in acinar cells (as previously reported in ref. 34) and at a lower level in endocrine cells (Figure 5C). Immunostaining of ANXA2 was also performed on isolated cadaveric human islets derived from 2 separate donors (Figure 5D). Although isolated islets displayed a great variability in their staining pattern, the highest ANXA2 protein levels were detected at the plasma membrane, with some islets showing increased abundance in cells along the islet periphery, a pattern reminiscent of that seen in *ZNF148*-KO eBC. Thus, endogenous human islets show an ANXA2 protein localization pattern similar to that of *ZNF148*-KO eBC but not control eBC.

To determine if the perturbed, nuclear localization of ANXA2 in control eBC was restricted to a specific human embryonic stem cell (hESC) line, we tested eBC generated from the episomal reprogrammed human induced pluripotent stem cell (iPSC) line using the same differentiation protocol. Due to the lack of the INS/GFP reporter in the iPSC line, we utilized custom antibodies against cell surface molecules

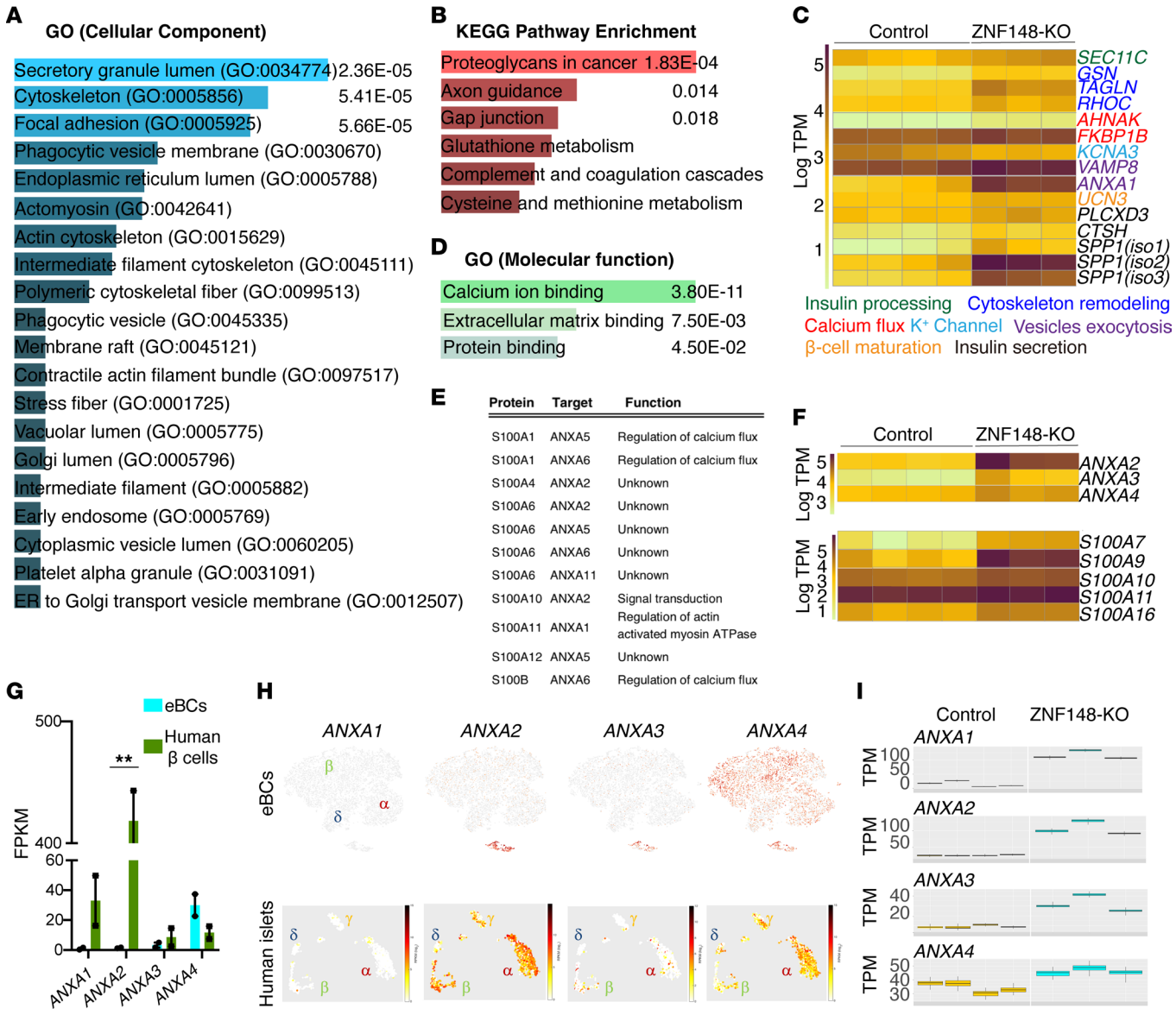


**Figure 4. Loss of *ZNF148* increases expression of annexin and S100 genes.** (**A**) List of subcellular areas enriched in differentially expressed (DE) genes identified by RNA-Seq, identified by cellular component Gene Ontology analysis. See also Supplemental Table 2. (**B**) List of enriched KEGG pathways. See also Supplemental Table 3. (**C**) Heatmap of selected DE genes reported to be involved in insulin secretion and corresponding functional role. (**D**) Selected molecular functions enriched in DE genes, identified by Gene Ontology analysis. (**E**) List of validated S100-annexin protein interactions and their reported molecular function. (**F**) Heatmap of annexin and S100 genes differentially expressed between control and *ZNF148*-KO eBC. (**G**) Expression (as measured by RNA-Seq) of *ANXA1*, *ANXA2*, *ANXA3*, and *ANXA4* in eBC and endogenous β cells isolated from human islets by FACS. Data presented as mean ± SD; $n = 2$ independent samples. $^{**}P < 0.01$. (**H**) Cells expressing *ANXA1*, *ANXA2*, *ANXA3*, and *ANXA4* in eBC (top panel) and human islets (bottom panel); expression levels shown as heatmap of $\log_2$ expression as measured by single-cell RNA-Seq. Subpopulations of α cells, β cells, and δ cells are indicated. (**I**) Expression levels of *ANXA1*, *ANXA2*, *ANXA3*, and *ANXA4* in control and *ZNF148*-KO eBC as measured by RNA-Seq. TPM, transcripts per million.

to enrich for endocrine progenitors using magnetic-activated cell sorting (MACS), and we generated iPSC-derived islet-like clusters (52). Analysis of ANXA2 expression in iPSC-derived islet-like clusters showed nuclear localization (Figure 5E) indistinguishable from the pattern observed in hESC-derived eBC. These findings suggest that the lack of membrane translocation of ANXA2 observed in SC–β cells is conserved in genetically different stem cell lines and is, thus, a common characteristic of islet-like clusters differentiated under our in vitro conditions. Furthermore, these data support that loss of ZNF148 increases translocation of ANXA1 and ANXA2 to the plasma membranes.

*Loss of ZNF148 enhances translocation of annexin A2 through activation of S100A16.* To investigate a potential direct role for ZNF148 in the regulation of annexin-S100 complexes, we used Harmonizome (53) to

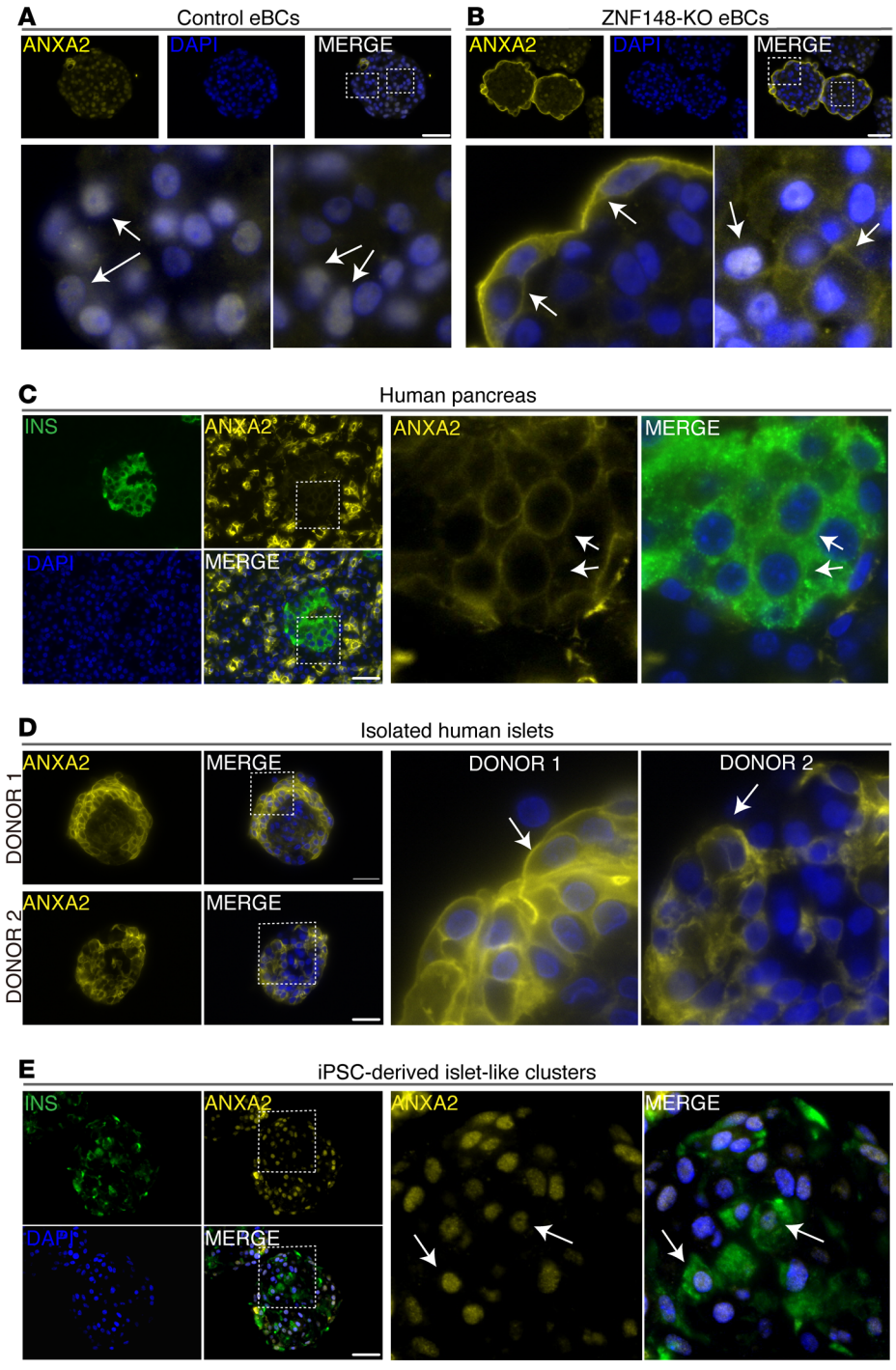


**Figure 5. Loss of *ZNF148* affects membrane localization of annexins.** (**A**) Immunofluorescence staining of ANXA2 (yellow) and DAPI (blue) in control eBC. Scale bar: 50 μm. Boxed areas are magnified (8×) below, and white arrows indicate prominent nuclear localization of ANXA2 in control eBC. (**B**) Immunofluorescence staining of ANXA2 (yellow) and DAPI (blue) in ZNF148-KO eBC. Scale bar: 50 μm. Boxed areas are magnified (8×) below, and white arrows indicate prominent membrane localization of ANXA2 in *ZNF148*-KO eBC. (**C**) Immunofluorescence staining of ANXA2 (yellow) and INS (green) in human pancreatic sections. Scale bar: 50 μm. Boxed areas are magnified (6×) to the right, and white arrows indicate prominent membrane localization of ANXA2 in β cells. *n* = 5 independent samples. (**D**) Immunofluorescence staining of ANXA2 (yellow) in isolated cadaveric islets of 2 donors. Scale bar: 50 μm. Boxed areas are magnified (6×) to the right, and white arrows indicate prominent membrane localization of ANXA2. (**E**) Immunofluorescence staining of ANXA2 (yellow) and INS (green) in iPSC-derived islet-like clusters. Scale bar: 50 μm. Boxed areas are magnified (5×) to the right, and white arrows indicate prominent nuclear localization of ANXA2.

predict ZNF148's target genes based on known ZNF148 binding site motifs from the TRANSFAC database (53). This analysis identified *S100A4*, *S100A5*, *S100A13*, *S100A16*, and *S100B* as potential target genes for ZNF148 (Figure 6A). Among these S100 genes, *S100A16* was the only one upregulated in *ZNF148*-KO eBC (Figure 6B and Figure 4F). To explore whether ZNF148 directly regulates expression of *S100A16* in the context of endogenous human islets, we performed ChIP-qPCR from 20,000 human islets equivalent (IEQs). ChIP-qPCR was performed on the region surrounding the predicted binding site for ZNF148 (Figure 6C). A previously validated ZNF148 target gene (*GAST*) was used as positive control (Figure 6D), and myoglobin served as negative control. The recovery for *S100A16*, expressed as a percentage of input, was similar to that of *GAST* (Figure 6E), indicating that ZNF148 directly binds to the *S100A16* locus, resulting in reduced *S100A16* expression. Since the ChIP-qPCR analysis demonstrated a direct link between ZNF148 protein and *S100A16* gene, we asked if overexpression of *S100A16* in the presence of exogenous ANXA2 is sufficient to recapitulate the translocation observed in the *ZNF148*-KO eBC. To test this hypothesis, we generated a doxycycline (DOX) inducible *S100A16* overexpression clonal line on the $INS^{GFP/w}$ background (Figure 6F). Five clones were screened for efficient *S100A16* expression in the presence or absence of DOX (Supplemental Figure 5, A and B), and 2 clones (expressing different levels of *S100A16*) were used for the generation of eBC.

First, we set out to test the optimal time points for DOX induction of S100A16 overexpression. Continuous DOX treatment from both the definitive endoderm stage (day 2) or the pancreatic progenitor stage (day 12) impaired the generation of INS/$GFP^+$ β cells (Supplemental Figure 5, C–E, and Supplemental Figure 6). These inhibitory effects might be explained by the supraphysiological levels of *S100A16* that were approximately 400-fold over those for untreated clones in different DOX concentrations (Supplemental Figure 5, A and B), whereas expression of *S100A16* in *ZNF148*-KO eBC was only ~2-fold higher than in control eBCs (Figure 6B and Supplemental Table 1). Detrimental effects linked to overexpression of S100A16, including increased cell proliferation, have been previously observed in a preadipocyte cell model (54). Similarly, ectopic constitutive expression of *S100A16* at the definitive endoderm stage resulted in increased proliferation, morphological alteration of the clusters, and loss of insulin transcription (Supplemental Figure 5, D and E). Ectopic constitutive overexpression of *S100A16* at the pancreatic progenitor stage (Supplemental Figure 6A) also resulted in loss of insulin transcription (Supplemental Figure 6B), underscoring the detrimental effects of prolonged and excessive levels of S100A16 in developing β cells.

In order to minimize the length of *S100A16* expression, DOX treatment was started after eBC generation (Supplemental Figure 7A). Exogenous ANXA2 protein was added to the cultures for 2 days to mimic the increased expression observed in *ZNF148*-KO eBC. ANXA2 was predominately localized in nuclei before *S100A16* overexpression (Figure 6G). While an 8-hour DOX treatment at the eBC stage resulted in ANXA2 membrane and cytoplasm localization to a similar extent to what we observed in *ZNF148*-KO eBCs (Figure 6G), this treatment regimen still induced *S100A16* overexpression to 50-fold over controls (Supplemental Figure 7B). To achieve more physiological levels of *S100A16* expression mimicking those found in *ZNF148*-KO eBCs, we performed a time course analysis treating eBCs with DOX for different periods (5 minutes, 15 minutes, 30 minutes, 1 hour, 2 hours, 4 hours, and 8 hours). qPCR analysis revealed that 2-hour DOX treatment at the eBC stage achieved a 5-fold increase in *S100A16* expression compared with no-DOX controls (Supplemental Figure 7B). This physiological increase of S100A16 expression did not affect the INS/GFP signal in eBCs (Supplemental Figure 7C), and a DOX treatment regimen of 2 hours at the eBC stage was therefore chosen for subsequent perifusion experiments (Figure 6H). C-PEP secretion at the peak of the first phase (26 minutes) was increased in cells overexpressing S100A16 in the presence of exogenous ANXA1 or ANXA2 when compared with those without S100A16 overexpression and no additional ANXA1/ANXA2 treatment (–DOX, –ANXA2/ANXA1 vs. +DOX, +ANXA2, $P = 0.05$; –DOX, –ANXA2/ANXA1 vs. +DOX, +ANXA1, $P = 0.09$) (Figure 6I). Furthermore, eBCs overexpressing S100A16 together with exogenous ANXA1 or ANXA2 showed significantly higher AUC of C-PEP secretion between 18 and 40 minutes, a time frame that includes both first-phase and second-phase compared with cells without DOX and no additional ANXA2/ANXA1 (–DOX, –ANXA2/ANXA1 vs. +DOX, +ANXA2, $P = 0.01$; –DOX, –ANXA2/ANXA1 vs. +DOX, +ANXA1, $P = 0.01$) (Figure 6J). These data are consistent with the first- and second-phase secretion observed in *ZNF148*-KO and control eBCs (Figure 3D) and indicate that providing the right balance of S100A16 and ANXA proteins enhance GSIS.

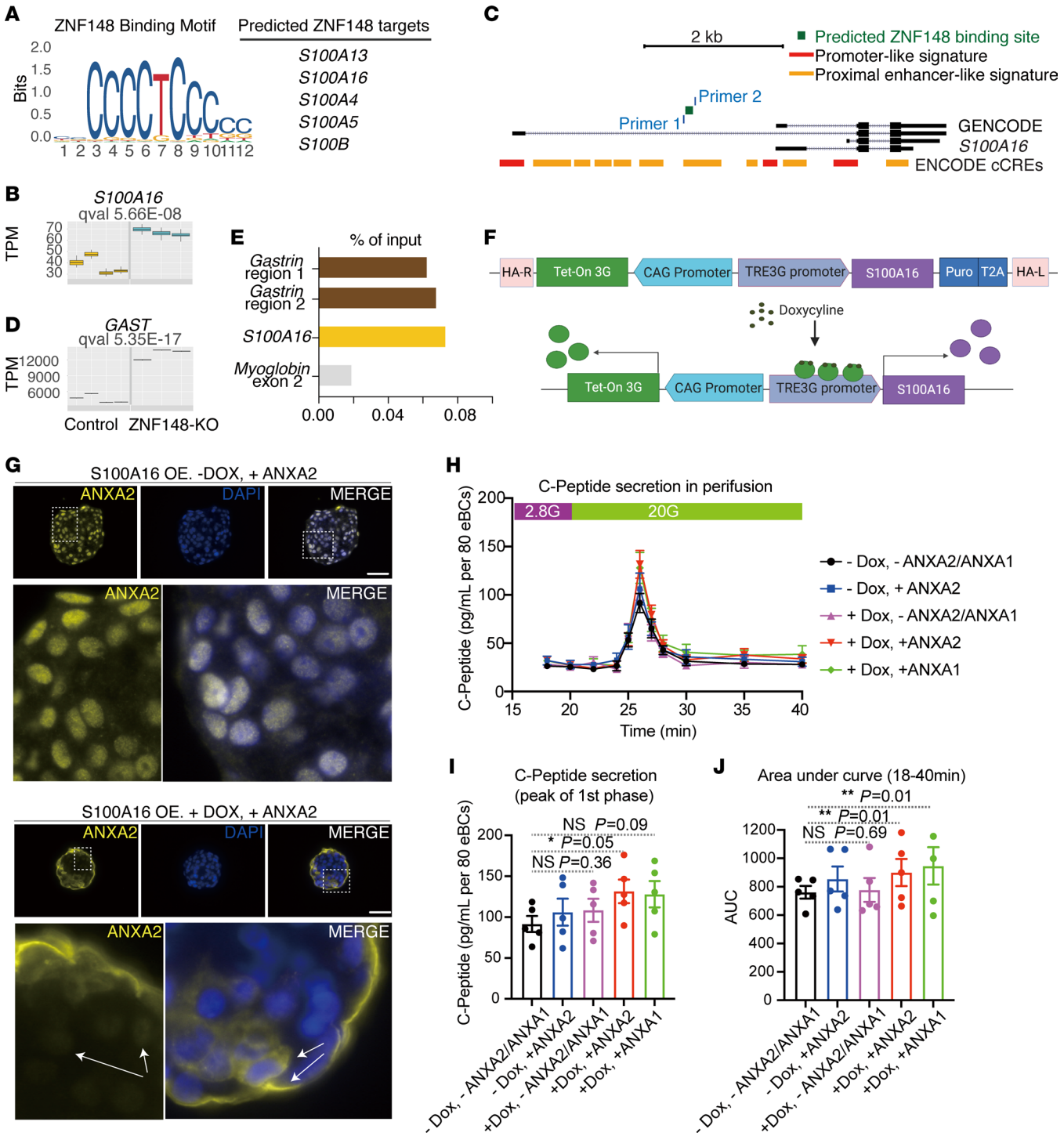


**Figure 6. Ectopic expression of *S100A16* mediates cellular translocation of annexin A2 and increased first-phase insulin secretion.** (**A**) ZNF148 binding site motifs from TRANSFAC and predicted ZNF148 targets from the S100 family. (**B**) RNA-Seq expression levels of *S100A16* in control and *ZNF148*-KO eBC. $n = 3$ independent samples. TPM, transcripts per million. (**C**) Schematic representation of *S100A16* locus. Predicted binding site for ZNF148 (green) and location of ChIP-qPCR primers. (**D**) RNA-Seq expression levels of *GAST* in control and *ZNF148*-KO eBC (clone A). $n = 3$ independent samples. (**E**) ChIP-qPCR quantification of DNA input recovery for gastrin (positive control), S100A16, and myoglobin (negative control) in 20,000 human IEQs. (**F**) Schematic representation of the DOX-inducible *S100A16* overexpression clonal line. (**G**) Immunofluorescence staining of ZNF148 (yellow) in eBC after treatment (48 hours) with exogenous ANXA2 alone (top panel, 6× magnification of the boxed area) or in combination with DOX treatment (8 hours) (bottom panel, 8× magnification of the boxed area). White arrows indicate prominent nuclear localization of ANXA2 in control eBC treated only with exogenous ANXA2 and prominent membrane and cytoplasmic localization in DOX/ANXA2-treated eBC. DAPI staining depicts nuclei (blue). Scale bar: 50 μm. (**H**) Dynamic glucose-stimulated C-peptide secretion in eBCs treated with or without DOX to stimulate S100A16 expression and with or without ANXA2/ANXA1 ($n = 5$ for each group; 80 eBCs each group). (**I**) C-peptide secretion at the peak of first-phase secretion (26 minutes) in each of the groups shown in **H**. $n = 5$ for each group. (**J**) AUC of C-peptide secretion from 2.8 mM basal low and 2 0mM high glucose incubation shown in **H**. $n = 5$ for each group. Data are presented as mean ± SEM. $^*P < 0.05$; $^{**}P < 0.01$; $^{***}P < 0.001$; NS, not significant determined by 2-tailed unpaired Student's *t* test.

*Loss of ZNF148 affects distribution of insulin granules in SC–β cells*. The key role of annexins in vesicle trafficking has been extensively investigated (15, 16, 21, 55–57). To test whether loss of *ZNF148* alters the number of secretory granules and/or their intracellular distribution, we performed soft x-ray tomography (58, 59) to generate 3D reconstructions of control eBC and *ZNF148*-KO eBC at low stimulatory glucose (2.8 mM), and after 30 minutes of incubation at high stimulatory glucose (20 mM). The differential x-ray absorption of each type of organelle allows for the detection and quantification of organelles based on their native contrast and without staining. Specifically, soft x-ray tomography allows the identification of plasma membrane, nucleus, nucleolus, mitochondria, and secretory granules (Figure 7A), as shown in previous studies (58).

No significant differences were observed between control and *ZNF148*-KO eBC in terms of insulin granule x-ray absorption, indicating no significant difference in the molecular density of the insulin granules (Figure 7A). Each voxel in the reconstructed tomogram gives quantitative information about the density of bio-organic components in each single subcellular compartment (60, 61). Each tomogram provided information about the amount of insulin granule per cell volume and their distribution within each cell. The detection of insulin granules was conducted automatically, as reported in Methods. Although the normalized insulin vesicle number did not reach statistical significance (Figure 7B), a detailed analysis of the distribution of the insulin granules relative to the plasma membrane showed a significant difference in unstimulated control eBC and *ZNF148*-KO eBC (2.8 mM). The insulin granule signal in control eBC was predominately found close to the plasma membrane (Figure 7C), whereas *ZNF148*-KO eBC displayed a similar mean granule response close to the plasma membrane and increased granule signals in the interior of the cell. These data show that loss of *ZNF148* is linked to alteration of insulin granule localization.

*Loss of ZNF148 increases insulin secretion in primary human islets*. The changes in kinetics of insulin secretion observed in *ZNF148*-KO eBC partially recapitulated the observations in the β-*Zfp148*$^{KO}$ mice (26). Although *ZNF148*-KO eBC show increased secretion during the second phase, they lack enhanced secretion during the acute first phase. Considering the bottleneck in glycolysis observed in our SC–β cells, we asked whether endogenous human islets would recapitulate the enhanced secretion observed in β-*Zfp148*$^{KO}$ mice during the first-phase secretion. To test if loss of *ZNF148* enhances insulin secretion in human islets, we performed siRNA-mediated downregulation of *ZNF148* on cadaveric islets from 2 separate donors and compared their secretion kinetics by GSIS (Figure 8A). Partial downregulation (~50%; Figure 8F) resulted in a significant increase of insulin secretion primarily during the acute first phase (Figure 8, B and C). The temporal dynamic was also affected, with glucose sensitivity via glucose ramp assays in *ZNF148*-knockdown islets (Figure 8D). *ZNF148*-knockdown human islets showed an increased, albeit not statistically significant, response at 3 mM glucose. However, *ZNF148*-knockdown islet did secrete C-PEP at significantly higher levels than the scramble siRNA–treated control group at 5 mM glucose. After calculating the AUC of C-PEP secretion in each segment of specific glucose concentration, *ZNF148*-knockdown islets exhibit significantly higher AUC of C-PEP secretion in 3 mM, 5 mM, 7 mM, and 15 mM glucose stimulation than that of scramble siRNA–treated control group (Figure 8E). The glucose ramp data, therefore, demonstrate higher glucose sensitivity of *ZNF148*-knockdown human islets and, overall, further support the hypothesis that *ZNF148* plays a negative role in insulin secretion and human islet metabolism.

In summary, we report a general role for *ZNF148* in negatively affecting insulin secretion in human islets and additional roles in regulating membrane dynamics in in vitro generated SC–β cells. Specifically, we describe how loss of *ZNF148* restores the proper localization of annexin proteins at plasma membranes in SC–β cells, a process that has been shown to be involved in the formation of membrane bridges necessary for docking of insulin vesicles. Our analysis provides evidence for how deregulation of *ZNF148* perturbs levels of annexin-S100 complexes at plasma membranes of β cells, opening a possible therapeutic approach for T2D.

## Discussion

*ZNF148* has only recently emerged as a regulator of pancreatic β cell function. In 2019, we (26) discovered that mice with a β cell–specific loss of the homologous *Zfp148* displayed enhanced glucose tolerance, and ex vivo cultured islets from these mice were able to secret higher levels of insulin. Here, we show that reduction of *ZNF148* in human cadaveric islets and ablation of *ZNF148* in SC–β cells also results in increased insulin secretion. Each model system recapitulates aspects of the phenotype observed in the β-*Zfp148*$^{KO}$ mice and affirms *ZNF148* as a repressor of insulin secretion in human β cells.

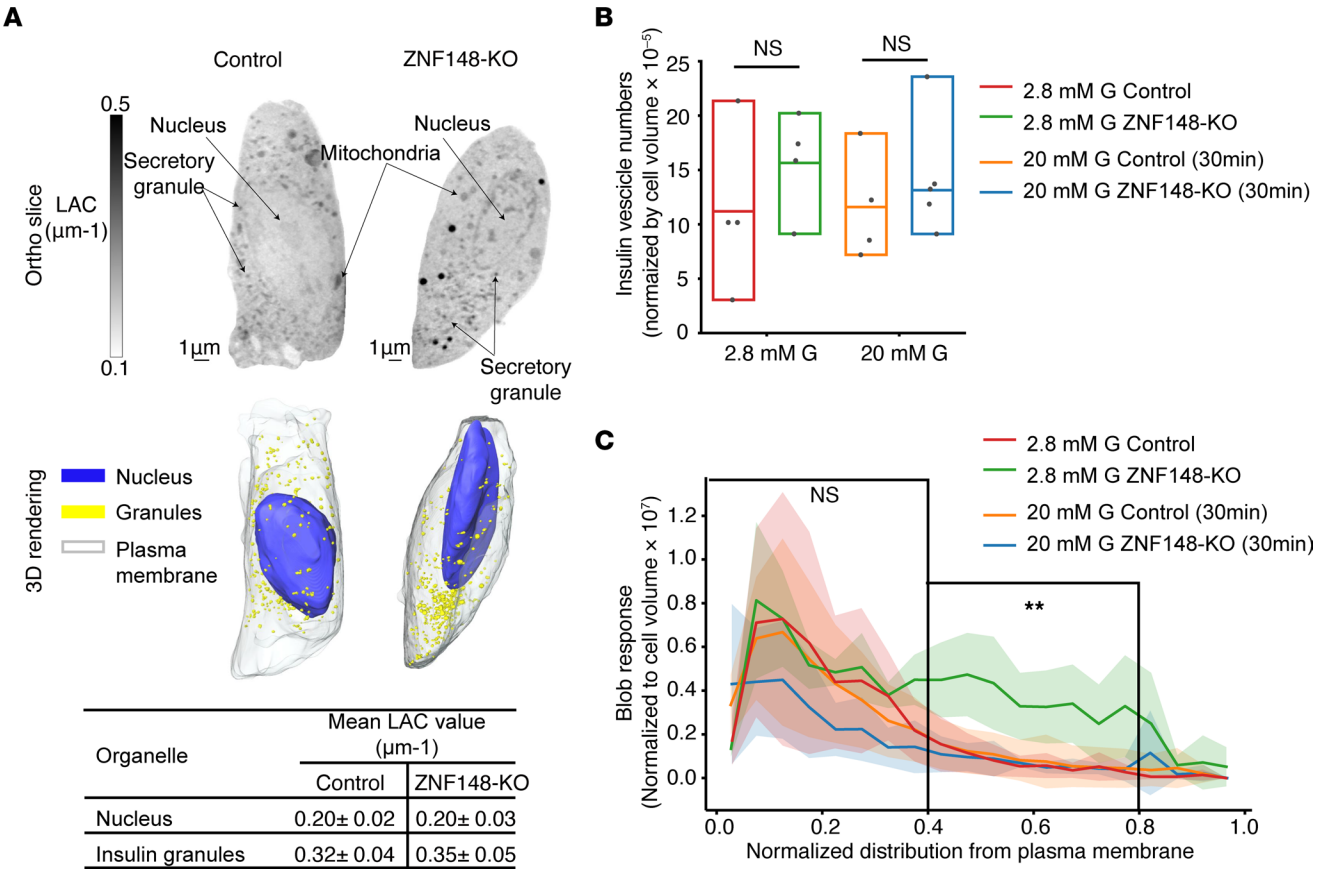


| Organelle | Mean LAC value (µm-1) | |
|---|---|---|
| | Control | ZNF148-KO |
| Nucleus | 0.20± 0.02 | 0.20± 0.03 |
| Insulin granules | 0.32± 0.04 | 0.35± 0.05 |

**Figure 7. Glucose stimulation effects on distribution of insulin granules in SC–β cells by x-ray tomography.** (**A**) Morphological analysis of insulin vesicle distribution in individual eBC. (Top) Single ortho-slices of control (left) and *ZNF148*-KO eBC (right) after 30 minutes of stimulation with 2.8 mM glucose. Organelles are represented by different levels of grey values, with a threshold between 0.1 and 0.5 (1/µm). Black arrows indicate cell nucleus, mitochondrial network, and insulin vesicles. (Middle) A 3D rendering of the segmented organelles in individual eBC. The nucleus is marked in blue, insulin vesicles in yellow, and the plasma membrane is highlighted in white. (Bottom) Average x-ray absorption coefficient (LAC) values for nucleus and insulin vesicles in control and *ZNF148*-KO eBC. (**B**) Representative insulin granule number normalized by cell volume. No significant difference is detected between any of the different treatments. (**C**) Plot representing the granule response distribution per condition. No significant difference is visible for the spatial distribution between cells treated with 20 mM glucose. Conversely, at 2.8 mM glucose, granules in *ZNF148*-KO and control eBC show a clear difference in the distribution from the plasma membrane within the threshold of 0.4 and 0.8. Two-tailed Student's *t* test. $^{**}P < 0.01$.

However, despite the similarities, we did note differences in the effect of *ZNF148* reduction versus ablation in primary and SC–β cells, respectively. Second-phase but not first-phase insulin secretion was enhanced in the SC–β cell model. Primary islets presented with an increase in first-phase secretion, but enhanced secretion in the second phase did not reach statistical significance. These disparities are likely due to the different experimental systems, such as partial knockdown versus complete ablation, but also reflect inherent differences in SC–β cells compared with primary β cells as discussed below.

We (3) and others (62) have previously reported that SC–β cells are able to release insulin in response to glucose, but the magnitude and the dynamic of secretion are not identical to those observed in cadaveric human islets. Specifically, defects in sustaining insulin secretion during the second phase have been noted. Second-phase secretion requires the trafficking of granules from the reserve pool (RP) to the plasma membrane. Recently, Hogrebe and colleagues (63) suggested that a way to improve first- and second-phase GSIS is by modulating the state of the actin cytoskeleton to drive pancreatic lineage specification. Meanwhile, Davis and colleagues (35) identified a defect in glucose metabolism that, once overcome, allows glucose-sensing and insulin secretion comparable with endogenous human islets. These studies highlighted deficiencies of the most current generation of SC–β cells.

We first tested whether *ZNF148* elimination might reverse metabolic defects in our SC–β cells. While we were able to confirm impaired metabolite flux previously described by Davis and colleagues (35) in SC–β cells generated with our differentiation protocol, elimination of *ZNF148* did not restore normal glycolytic

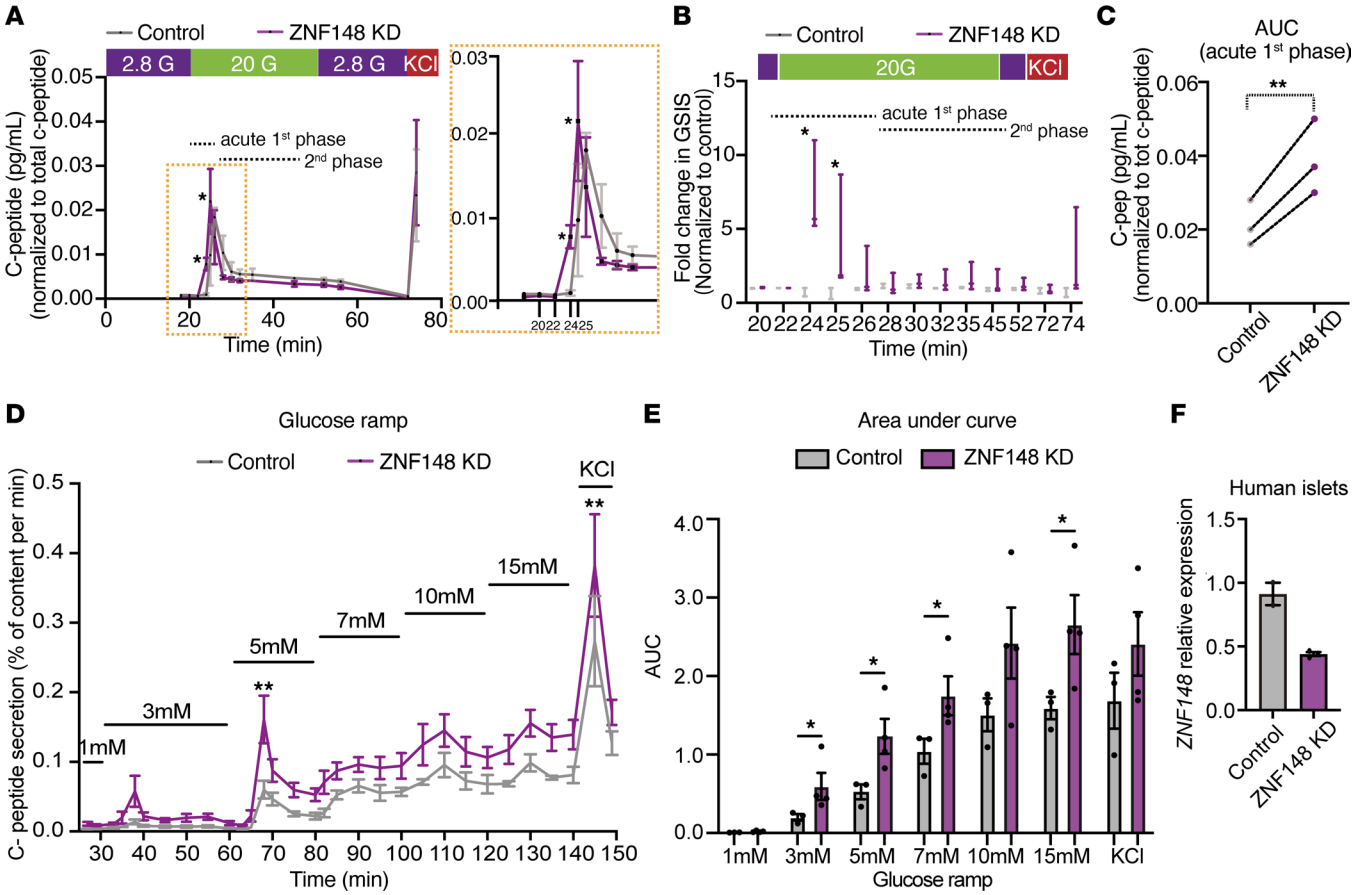


**Figure 8. Effects of *ZNF148* downregulation on insulin secretion in human islets.** (**A**) Dynamic secretion of C-peptide in response to stimulation with 20 mM glucose and 30 mM KCl, starting with basal glucose concentration of 2.8 mM, in control cadaveric islets (80 islets) and islets treated with siRNA targeting *ZNF148* (80 islets). Inset picture shows secretion during the acute first phase. $n = 3$. $^*P < 0.05$ determined by 2-tailed $t$ test. (**B**) Dynamic secretion of C-peptide in control cadaveric islets and islets treated with siRNA targeting *ZNF148*. Data are presented as mean of fold change (20 mM/2.8 mM) relative to control islets. $n = 3$. (**C**) Dynamic secretion of C-peptide during acute first phase secretion (minute 22–26) in control cadaveric islets and islets treated with siRNA targeting *ZNF148*. Data are presented as AUC. Dotted line indicates islets from the same biological sample. (**D**) C-peptide secretion of *ZNF148* knockdown ($n = 4$) and scramble control ($n = 3$) human islets normalized to total C-peptide content per minute upon the ramp up glucose challenge. (**E**) AUC of C-peptide secretion shown in **D** of *ZNF148* knockdown ($n = 4$) and scramble control ($n = 3$) human islets. (**F**) Relative *ZNF148* gene expression of *ZNF148*-knockdown ($n = 3$) and scramble control ($n = 2$) human islets. Data are presented as mean ± SEM. $^*P < 0.05$, $^{**}P < 0.01$ determined by 2-tailed $t$ test.

flux, thus eliminating this aspect as the underlying mechanism for *ZNF148* function. In contrast, we found that our SC–β cells lacking *ZNF148* regain some aspects of membrane dynamics that are characteristic of cadaveric human islets. Specifically, loss of *ZNF148* affects the expression levels of many annexin and S100 genes (Figure 4F) and the subcellular localization of annexin proteins (Figure 5). Annexin proteins are highly abundant in human islets (Figure 4, G and H) and are mainly localized to the plasma membrane. Annexins have been shown to be involved in regulation of actin filaments, reorganization of cytoskeleton, and formation of membrane bridges necessary for docking of insulin vesicles. Specifically, annexin A2 is a calcium-binding, actin-binding, and lipid-binding protein implicated in vesicle trafficking and exocytosis (15, 16, 18, 19, 21, 56). Previous studies have shown the importance of F-actin in insulin release (41). F-actin remodeling enables the redistribution of insulin granules to the periphery of the cell, and current models suggest that glucose-induced F-actin remodeling is key for granule mobilization. Moreover, a number of studies have shown that annexin proteins are also involved in the formation of a variety of granules. ANXA1 has been shown to contribute to the formation of granules in mast cells (64), whereas ANXA2 has been shown to be involved in the formation of Birbeck granules in Langerhans cells (65).

Our findings now provide a mechanistic model of *ZNF148* function by linking repressive function of the transcription factor to cellular localization of annexin proteins, distribution of vesicles, and consequently insulin secretion in human β cells. We pose that the translocation of annexin A2 from the nucleus to the

plasma membrane observed in our *ZNF148*-KO eBC is key for the increased secretion detected between the first and second phase in our SC–β cells cell model (Figure 3F). Annexins form heterotetramers with S100 proteins, a prerequisite for their function in mediating vesicle transport and membrane docking. Deletion of *ZNF148* relieves the transcriptional inhibition of *S100A16*, resulting in translocation of annexin A2 from the nucleus to the membrane, mediated by the formation of heterotetrameric complexes with S100A16. In support of this hypothesis, we show that insulin granule distribution is also affected in *ZNF148*-KO eBC. We observe a larger number of vesicles slightly farther away from the plasma membrane in *ZNF148*-KO β cells (Figure 7C) and a trend toward fewer docked granules in *ZNF148*-KO eBC after 30 minutes of stimulation with 20 mM glucose. These data indicate that elimination of *ZNF148* increases the pool of insulin vesicles that dock with the plasma membrane during the second-phase insulin secretion.

A number of additional questions arise from our work. Out of all the S100 genes deregulated following elimination of *ZNF148*, *S100A16* is the only predicted direct target, and ChIP analysis showed direct binding of ZNF148 to *S100A16* promoter in endogenous human islets (Figure 6E). Nevertheless, we cannot rule out the possibility that other S100 proteins with elevated expression in *ZNF148*-KO cells (Figure 4F) are also involved in the translocation of ANXA2. Neither can we exclude that the phenotypic effect observed is exclusively due to ANXA2, given the increased expression of ANXA1 (Figure 4I) and the interaction between annexin and S100 proteins (Figure 4E). Importantly, we observed that overexpressing S100A16 within physiological levels could improve insulin secretion when exogenous ANXA1/ANXA2 proteins are present as well (Figure 6, H–J, and Supplemental Figure 7), indicating that providing the right balance of these factors enhances insulin secretion properties. Although we were able to demonstrate the shift in localization of ANXA2 from the nucleus to the plasma membrane, we cannot exclude that other *ZNF148* target genes may be partially responsible for the secretion phenotype. Our differential expression analysis revealed that many genes known to be involved in insulin processing, cytoskeleton remodeling, calcium flux, vesicles exocytosis, and β cell maturation (Figure 4C and Supplemental Table 1) were also upregulated.

In summary, our findings extend prior work by describing a model by which *ZNF148* curbs insulin secretion in human pancreatic β cells via limiting essential annexin/S100-mediated localization of insulin vesicles. Further defining the exact role of *ZNF148* could reveal insights into optimizing the functionality of SC–β cells and could also lead to novel T2D therapies aimed at improving β cell function.

## Methods

Supplemental Methods are available online with this article.

*Cell culture*. hESC line MEL-1 (NIH registration no. 0139, sex of cells was male), with a GFP reporter knocked into 1 allele of *INS* locus (Mel1 $INS^{GFP/W}$, originally obtained from S.J. Micallef and E.G. Stanley; ref. 66). Mel1 $INS^{GFP/W}$ were cultured on irradiated mouse embryonic fibroblasts (MEFs; Thermo Fisher Scientific) in hESC media (DMEM/F12, 20% KOSR [Thermo Fisher Scientific], nonessential amino acids [NEAA; Thermo Fisher Scientific], Glutamax [Thermo Fisher Scientific], 2-mercaptoethanol [MilliporeSigma], and 10 ng/mL recombinant human FGF2 [R&D Systems]). The human iPSC line was obtained from Thermo Fisher Scientific (catalog A18945).

*Human islets*. Human islets used for siRNA experiments were obtained from the UCSF Islet Core. Human islets used for ChIP-qPCR experiments were obtained from PRODO Laboratories. Isolated islets were recovered in PRODO islet media [PIM(S), PIM(G), and PIM(ABS)] for 24 hours prior to functional analysis. The procurement and use of human islets utilized in this study was approved by the institutional biosafety committee at UCSF.

*Immunofluorescence staining*. Cadaveric islets and SC–β cells at indicated stages of differentiation were fixed with 4% paraformaldehyde (PFA) for 15 minutes at room temperature, washed with 1× PBS, and stored at 4°C until processing for paraffin sectioning. Clusters or cadaveric islets were first embedded in 2% agar, followed by dehydration, paraffin embedding, and sectioning at 5 μm thickness. Sections were then stained as previously described (2). Primary antibodies (antigen, species, dilution, manufacturer) included: ZNF148 (rabbit, 1:50, LS-C358401, LSBio); ANXA1 (rabbit, 1:500, 11256-1-AP, Thermo Fisher Scientific); ANXA2 (rabbit, 1:500, 71-3400, Thermo Fisher Scientific); ANXA3 (rabbit, 1:500, NBP1-90155, Novus Biologicals); and insulin (guinea pig, 1:500, DAKO, A0564). Secondary antibodies of appropriate species from Invitrogen were used at 1:500 dilution: donkey anti–rabbit IgG (H+L) Alexa Fluor 488 (catalog A21206), donkey anti–rabbit IgG (H+L) Alexa Fluor 555 (catalog A31572), and goat anti–guinea pig IgG (H+L) Alexa Fluor 488 (catalog A11073). Cells were counterstained with DAPI to mark nuclei.

Slides were mounted with coverslips using Prolong Diamond Antifade reagent (Invitrogen). Images were generated using Zeiss apotome.

*Flow cytometry*. For intracellular staining, SC–β cells at indicated stages were dissociated in single cells using Accumax for 8–10 minutes at 37°C, fixed with 4% PFA for 15 minutes at room temperature, permeabilized, and stained for various intracellular markers. The following directly conjugated antibodies were used: NKX6.1-Alexa Fluor 647 (563338, BD Bioscience, 1:50); PDX1-PE (562161, BD Bioscience, 1:40); and C-PEP-488 (C-PEP-01 Chemicon, conjugated in house, 1:200). For GFP-live staining, single cells were directly analyzed by flow cytometry after dissociation in Accumax and resuspension in FACS media. Cells were sorted by FACSARIA II, FACSARIA III, or FACSARIA Fusion. Data were analyzed using FlowJo.

*Dynamic and static GSIS*. A perifusion system from Biorep Technologies was used for dynamic secretion assays. In total, 80–100 eBCs or 70–100 human islets were sandwiched between 2 layers of Bio-Gel P4 Polyacrylamide beads (BioRad, 150-4124) and placed on filters in plastic chambers. Under temperature-controlled (37°C) and $CO_2$-controlled conditions, the clusters were perifused at 100 μL/min with KRB buffer (137 mM NaCl, 4.7 mM KCl, 1.2 mM $KH_2PO_4$, 1.2 mM $MgSO_4$, 2.5 mM $CaCl_2$, 25 mM $NaCO_3$, 20 mM HEPES, 0.25% BSA filtered [pH 7.4]) using a peristaltic pump. After an initial 2-hour preincubation in 2.8 mM glucose-containing Krebs-Ringer bicarbonate (glucose-KRB) buffer, alternating low (2.8 mM) and high (20 mM) amounts of glucose with or without 30 mM KCl were perfused through the system. Flow-through was collected over the course of the experiment in 96-well plates containing proteinase inhibitor cocktail (Roche). At the end of the run, eBC/islets were recovered from the chambers, and total insulin was extracted by acid-ethanol overnight, followed by neutralization with Tris-HCl. Static secretion was performed using 100 eBC placed in round-bottom polypropylene 15 mL conical tubes, under temperature-controlled conditions (37°C) and with constant orbital shaking. After an initial 2-hour preincubation in 200 μL of 2.8 mM glucose-KRB, eBC were treated for 30 minutes at low glucose (2.8 mM), followed by 30 minutes in high glucose (20 mM), 30 minutes of low glucose, and 5 minutes in high glucose with 30 mM KCl. In total, 200 μL of media was collected after each incubation, and total insulin was recovered from eBC by extraction in acid-ethanol. C-PEP levels were measured using the STELLUX Chemi Human C-PEP ELISA kit (Alpco).

*Statistics*. Data are derived from at least 3 independent biological replicates, unless otherwise specifically indicated. Data are presented as mean ± SEM, unless otherwise specifically indicated. *P* values were calculated by 2-tailed unpaired Student's *t* test if not otherwise specifically indicated. $P < 0.05$ was considered significant. Statistical analyses were performed using GraphPad Prism 9.

*Study approval*. All experiments related to hESCs and iPSCs were performed using protocols approved by Human Gamete, Embryo, and Stem Cell Research Committee of UCSF. Human islets for research were provided by Islet and Cellular Production Core of UCSF.

## Author contributions

EDK conceived experiments, performed experiments, performed data analysis, interpreted results, and wrote the manuscript. YX performed experiments and data analysis, interpreted results, and edited the manuscript. CHE conceived, performed, and analyzed experiments for calcium oscillation studies and edited the manuscript. DIB performed immunofluorescent experiments. VL performed experiments and data analysis for soft x-ray tomography. AAE performed data analysis for soft x-ray tomography experiments. KLW counseled on soft x-ray tomography experiments. RLC performed experiments and data analysis for metabolic flux analysis. RGK performed data analysis for metabolic flux analysis experiments. MPK conceived experiments, performed data analysis, interpreted results, and edited the manuscript. ADA conceived experiments, interpreted results, and edited the manuscript. MH conceived experiments, interpreted results, and edited the manuscript.

## Acknowledgments

This work was supported by JDRF 3-PDF-2017-405-A-N to EDK. Work in the MH laboratory was supported by funds from the NIH (R01DK101573, R01DK105831). Work in the ADA laboratory was supported by funds from the NIH (DK101573, DK125961, and DK007665) and the American Diabetes Association (7-21-PDF-157). Work in the RGK laboratory was supported by funds from the NIH (DK127637). The National Center for X-ray Tomography is supported by funds from NIH (P41GM103445 and P30GM138441) and DOE's office of Biological and Environmental Research (DE-AC02-5CH11231).

Address correspondence to: Alan D. Attie, Departments of Biochemistry, Chemistry and Medicine, University of Wisconsin-Madison, 433 Babcock Dr., Madison, WI 53706, USA. Phone: 608.262.1372; Email: adattie@wisc.edu. Or to: Matthias Hebrok, Center for Organoid Systems and Tissue Engineering (COS), Technical University Munich (TUM), D-85748 Garching-Forschungszentrum, Germany. Phone: 49.8931.874.9707; Email: matthias.hebrok@tum.de.

MH's present addresses are: Center for Organoid Systems, Technical University Munich, Garching, Germany; Institute for Diabetes Organoid Technology, Helmholtz Munich, Helmholtz Diabetes Center, Neuherberg, Germany; and Munich Institute of Biomedical Engineering (MIBE), Technical University Munich, Munich, Germany.

1. Sneddon JB, et al. Stem cell therapies for treating diabetes: progress and remaining challenges. *Cell Stem Cell*. 2018;22(6):810–823.
2. Russ HA, et al. Controlled induction of human pancreatic progenitors produces functional beta-like cells in vitro. *EMBO J*. 2015;34(13):1759–1772.
3. Nair GG, et al. Recapitulating endocrine cell clustering in culture promotes maturation of human stem-cell-derived β cells. *Nat Cell Biol*. 2019;21(2):263–274.
4. Pagliuca FW, et al. Generation of functional human pancreatic β cells in vitro. *Cell*. 2014;159(2):428–439.
5. Rezania A, et al. Reversal of diabetes with insulin-producing cells derived in vitro from human pluripotent stem cells. *Nat Biotechnol*. 2014;32(11):1121–1133.
6. Ghazizadeh Z, et al. ROCKII inhibition promotes the maturation of human pancreatic beta-like cells. *Nat Commun*. 2017;8(1):298.
7. Yoshihara E, et al. ERRγ is required for the metabolic maturation of therapeutically functional glucose-responsive β cells. *Cell Metab*. 2016;23(4):622–634.
8. Veres A, et al. Charting cellular identity during human in vitro β cell differentiation. *Nature*. 2019;569(7756):368–373.
9. Mahaddalkar PU, et al. Generation of pancreatic β cells from CD177$^{+}$ anterior definitive endoderm. *Nat Biotechnol*. 2020;38(9):1061–1072.
10. Rosado-Olivieri EA, et al. YAP inhibition enhances the differentiation of functional stem cell-derived insulin-producing β cells. *Nat Commun*. 2019;10(1):1464.
11. Velazco-Cruz L, et al. Acquisition of dynamic function in human stem cell-derived β cells. *Stem Cell Reports*. 2019;12(2):351–365.
12. Henquin JC, et al. Dynamics of glucose-induced insulin secretion in normal human islets. *Am J Physiol Endocrinol Metab*. 2015;309(7):E640–E650.
13. Monastyrskaya K, et al. Annexins as intracellular calcium sensors. *Cell Calcium*. 2007;41(3):207–219.
14. Gerke V, et al. Annexins: linking $Ca^{2+}$ signalling to membrane dynamics. *Nat Rev Mol Cell Biol*. 2005;6(6):449–461.
15. Umbrecht-Jenck E, et al. S100A10-mediated translocation of annexin-A2 to SNARE proteins in adrenergic chromaffin cells undergoing exocytosis. *Traffic*. 2010;11(7):958–971.
16. Gabel M, et al. Phosphorylation cycling of Annexin A2 Tyr23 is critical for calcium-regulated exocytosis in neuroendocrine cells. *Biochim Biophys Acta Mol Cell Res*. 2019;1866(7):1207–1217.
17. Kang N, et al. Annexin I stimulates insulin secretion through regulation of cytoskeleton and PKC activity. *Anim Cells Syst (Seoul)*. 2009;13(1):17–23.
18. Hayes MJ, et al. Regulation of actin dynamics by annexin 2. *EMBO J*. 2006;25(9):1816–1826.
19. Grieve AG, et al. Annexin A2 at the interface of actin and membrane dynamics: a focus on its roles in endocytosis and cell polarization. *Int J Cell Biol*. 2012;2012:852430.
20. Benaud C, et al. AHNAK interaction with the annexin 2/S100A10 complex regulates cell membrane cytoarchitecture. *J Cell Biol*. 2004;164(1):133–144.
21. Gabel M, Chasserot-Golaz S. Annexin A2, an essential partner of the exocytotic process in chromaffin cells. *J Neurochem*. 2016;137(6):890–896.
22. Barwise JL, Walker JH. Annexins II, IV, V and VI relocate in response to rises in intracellular calcium in human foreskin fibroblasts. *J Cell Sci*. 1996;109 (pt 1):247–255.
23. Santamaria-Kisiel L, et al. Calcium-dependent and -independent interactions of the S100 protein family. *Biochem J*. 2006;396(2):201–214.
24. Weisz J, Uversky VN. Zooming into the dark side of human annexin-S100 complexes: dynamic alliance of flexible partners. *Int J Mol Sci*. 2020;21(16):5879.
25. Liu Y, et al. Annexin A2 complexes with S100 proteins: structure, function and pharmacological manipulation. *Br J Pharmacol*. 2015;172(7):1664–1676.
26. Keller MP, et al. Gene loci associated with insulin secretion in islets from non-diabetic mice. *J Clin Invest*. 2019;129(10):4419–4432.
27. Passantino R, et al. Negative regulation of beta enolase gene transcription in embryonic muscle is dependent upon a zinc finger factor that binds to the G-rich box within the muscle-specific enhancer. *J Biol Chem*. 1998;273(1):484–494.
28. Merchant JL, et al. ZBP-89, a Krüppel-like zinc finger protein, inhibits epidermal growth factor induction of the gastrin promoter. *Mol Cell Biol*. 1996;16(12):6644–6653.
29. Zou ZV, et al. Genomic profiling of the transcription factor Zfp148 and its impact on the p53 pathway. *Sci Rep*. 2020;10(1):14156.
30. Wang Y, et al. The ht beta gene encodes a novel CACCC box-binding protein that regulates T-cell receptor gene expression. *Mol Cell Biol*. 1993;13(9):5691–5701.

31. Taniuchi T, et al. Overexpression of ZBP-89, a zinc finger DNA binding protein, in gastric cancer. *Biochem Biophys Res Commun*. 1997;233(1):154–160.
32. Bakke J, et al. Transcription factor ZNF148 is a negative regulator of human muscle differentiation. *Sci Rep*. 2017;7(1):8138.
33. Schaum N, et al. Single-cell transcriptomics of 20 mouse organs creates a Tabula Muris. *Nature*. 2018;562(7727):367–372.
34. Segerstolpe Å, et al. Single-cell transcriptome profiling of human pancreatic islets in health and type 2 diabetes. *Cell Metab*. 2016;24(4):593–607.
35. Davis JC, et al. Glucose response by stem cell-derived β cells in vitro is inhibited by a bottleneck in glycolysis. *Cell Rep*. 2020;31(6):107623.
36. Alves TC, et al. Integrated, step-wise, mass-isotopomeric flux analysis of the TCA cycle. *Cell Metab*. 2015;22(5):936–947.
37. Jesinkey SR, et al. Mitochondrial GTP links nutrient sensing to β cell health, mitochondrial morphology, and insulin secretion independent of OxPhos. *Cell Rep*. 2019;28(3):759–772.
38. Westacott MJ, et al. Age-dependent decline in the coordinated [$Ca^{2+}$] and insulin secretory dynamics in human pancreatic islets. *Diabetes*. 2017;66(9):2436–2445.
39. Tomas A, et al. Regulation of pancreatic beta-cell insulin secretion by actin cytoskeleton remodelling: role of gelsolin and cooperation with the MAPK signalling pathway. *J Cell Sci*. 2006;119(pt 10):2156–2167.
40. Li J, et al. Quantitative phosphoproteomics revealed glucose-stimulated responses of islet associated with insulin secretion. *J Proteome Res*. 2015;14(11):4635–4646.
41. Wang Z, Thurmond DC. Mechanisms of biphasic insulin-granule exocytosis — roles of the cytoskeleton, small GTPases and SNARE proteins. *J Cell Sci*. 2009;122(pt 7):893–903.
42. Noguchi N, et al. FKBP12.6 disruption impairs glucose-induced insulin secretion. *Biochem Biophys Res Commun*. 2008;371(4):735–740.
43. Jacobson DA, Philipson LH. Action potentials and insulin secretion: new insights into the role of Kv channels. *Diabetes Obes Metab*. 2007;9 Suppl 2(suppl 2):89–98.
44. Zhu D, et al. Dual role of VAMP8 in regulating insulin exocytosis and islet β cell growth. *Cell Metab*. 2012;16(2):238–249.
45. Ohnishi M, et al. Involvement of annexin-I in glucose-induced insulin secretion in rat pancreatic islets. *Endocrinology*. 1995;136(6):2421–2426.
46. Liu M, et al. Proinsulin entry and transit through the endoplasmic reticulum in pancreatic beta cells. *Vitam Horm*. 2014;95:35–62.
47. Huang JL, et al. Genetic deletion of Urocortin 3 does not prevent functional maturation of beta cells. *J Endocrinol*. 2020;246(1):69–78.
48. Blum B, et al. Functional beta-cell maturation is marked by an increased glucose threshold and by expression of urocortin 3. *Nat Biotechnol*. 2012;30(3):261–264.
49. Cai M, et al. Role of osteopontin and its regulation in pancreatic islet. *Biochem Biophys Res Commun*. 2018;495(1):1426–1431.
50. Fløyel T, et al. CTSH regulates β cell function and disease progression in newly diagnosed type 1 diabetes patients. *Proc Natl Acad Sci U S A*. 2014;111(28):10305–10310.
51. Aljaibeji H, et al. Reduced expression of PLCXD3 associates with disruption of glucose sensing and insulin signaling in pancreatic β cells. *Front Endocrinol (Lausanne)*. 2019;10(735):735.
52. Parent AV, et al. Development of a scalable method to isolate subsets of stem cell-derived pancreatic islet cells. *Stem Cell Reports*. 2022;17(4):979–992.
53. Rouillard AD, et al. The harmonizome: a collection of processed datasets gathered to serve and mine knowledge about genes and proteins. *Database (oxford)*. 2016;2016:baw100.
54. Liu Y, et al. Identification of S100A16 as a novel adipogenesis promoting factor in 3T3-L1 cells. *Endocrinology*. 2011;152(3):903–911.
55. Pollard HB, et al. Role of intracellular proteins in the regulation of calcium action and transmitter release during exocytosis. *Monogr Neural Sci*. 1980;7:106–116.
56. Chasserot-Golaz S, et al. Annexin 2 promotes the formation of lipid microdomains required for calcium-regulated exocytosis of dense-core vesicles. *Mol Biol Cell*. 2005;16(3):1108–1119.
57. Cubells L, et al. Annexin A6-induced alterations in cholesterol transport and caveolin export from the Golgi complex. *Traffic*. 2007;8(11):1568–1589.
58. White KL, et al. Visualizing subcellular rearrangements in intact β cells using soft x-ray tomography. *Sci Adv*. 2020;6(50):eabc8262.
59. Le Gros MA, et al. X-ray tomography of whole cells. *Curr Opin Struct Biol*. 2005;15(5):593–600.
60. Do M, et al. Imaging and characterizing cells using tomography. *Arch Biochem Biophys*. 2015;581:111–121.
61. McDermott G, et al. Visualizing and quantifying cell phenotype using soft X-ray tomography. *Bioessays*. 2012;34(4):320–327.
62. Nair GG, et al. Emerging routes to the generation of functional β cells for diabetes mellitus cell therapy. *Nat Rev Endocrinol*. 2020;16(9):506–518.
63. Hogrebe NJ, et al. Targeting the cytoskeleton to direct pancreatic differentiation of human pluripotent stem cells. *Nat Biotechnol*. 2020;38(4):460–470.
64. Kim JY, et al. Granule formation in NGF-cultured mast cells is associated with expressions of pyruvate kinase type M2 and annexin I proteins. *Int Arch Allergy Immunol*. 2008;146(4):287–297.
65. Thornton SM, et al. The essential role of anxA2 in Langerhans cell Birbeck granules formation. *Cells*. 2020;9(4):974.
66. Micallef SJ, et al. INS(GFP/w) human embryonic stem cells facilitate isolation of in vitro derived insulin-producing cells. *Diabetologia*. 2012;55(3):694–706.